Joint Institute for Nuclear Research,
Dubna, September 99.

Extended Beam-Request 99 for COSY Proposal N20.

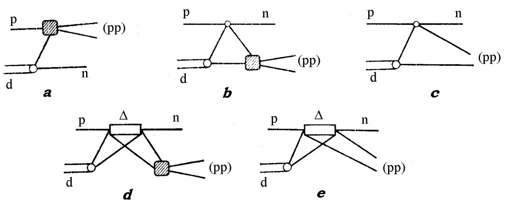

Figure 1: Mechanisms of the reaction $p + d \to n + (pp)$: a – one-nucleon exchange (ONE), b, c – single scattering (SS), d, e – double pN-scattering with excitation of the $\Delta-$isobar (Δ)

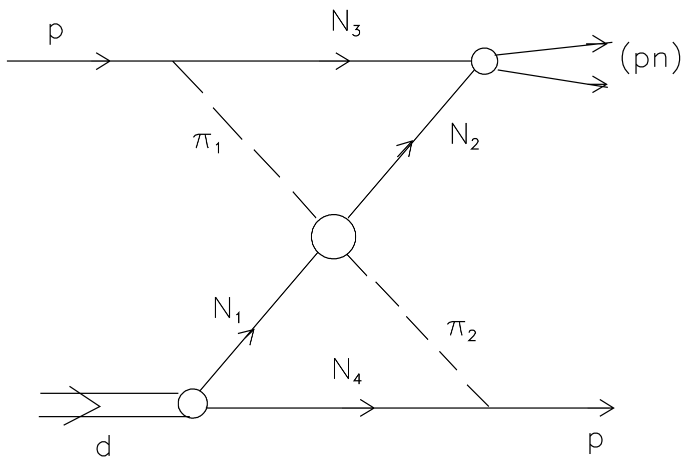

Figure 2: The mechanism of the process $pd \to p + (np)$ with a virtual meson (π, ρ, ω, $\eta \ldots$) in the intermediate state

Figure 11: empty11

Figure 12: empty12.a,b

Figure 13: empty13

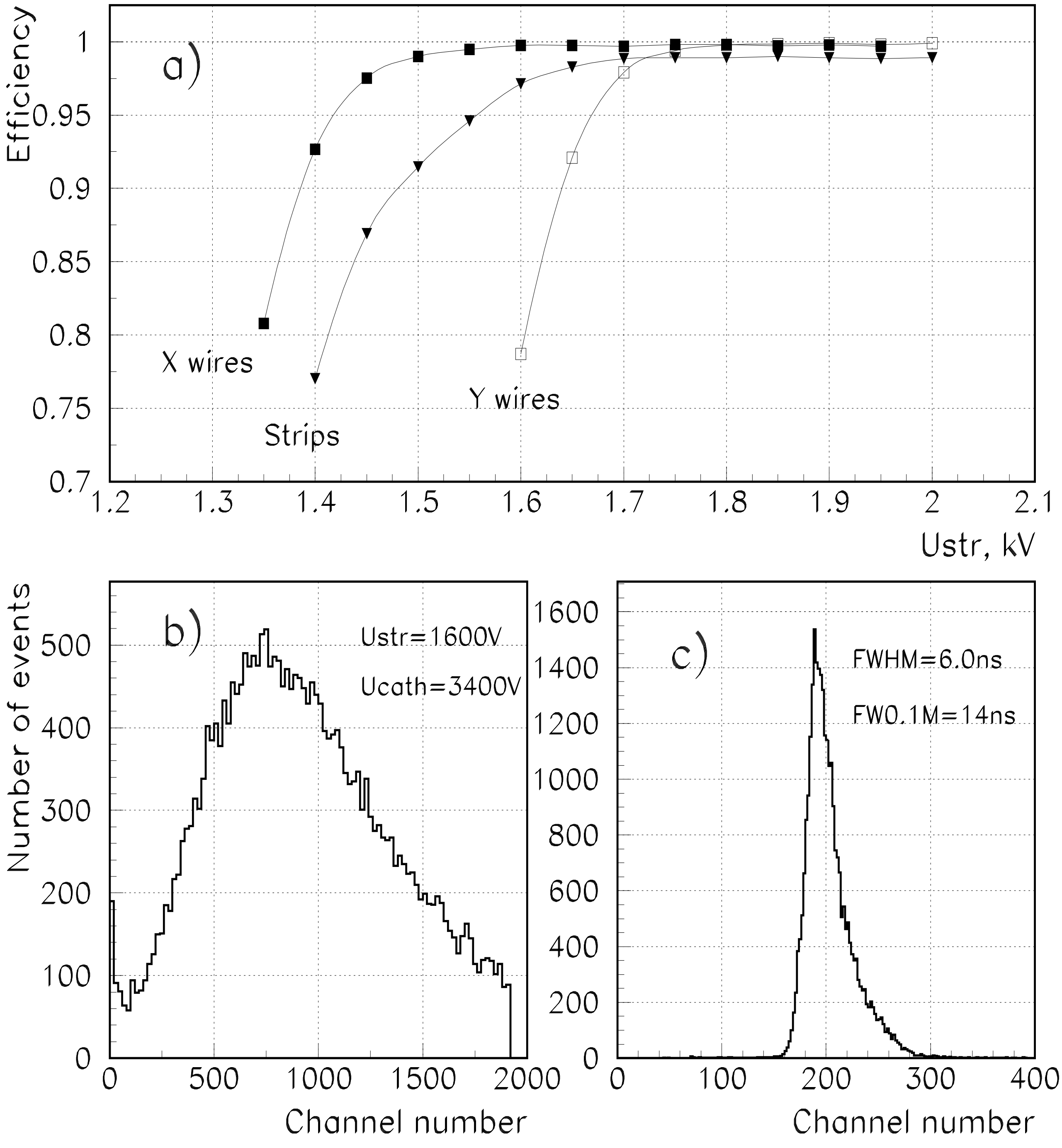

Figure 14: **Performance of the Forward multiwire proportional chambers FPC.**

a). Efficiency of X- and Y-wires and strips as a function of the voltage on the strip plane

b). Amplitude spectrum of signals from Y-wires.

c). Time spectrum of signals from a single wire. (One channel- 0.25ns.

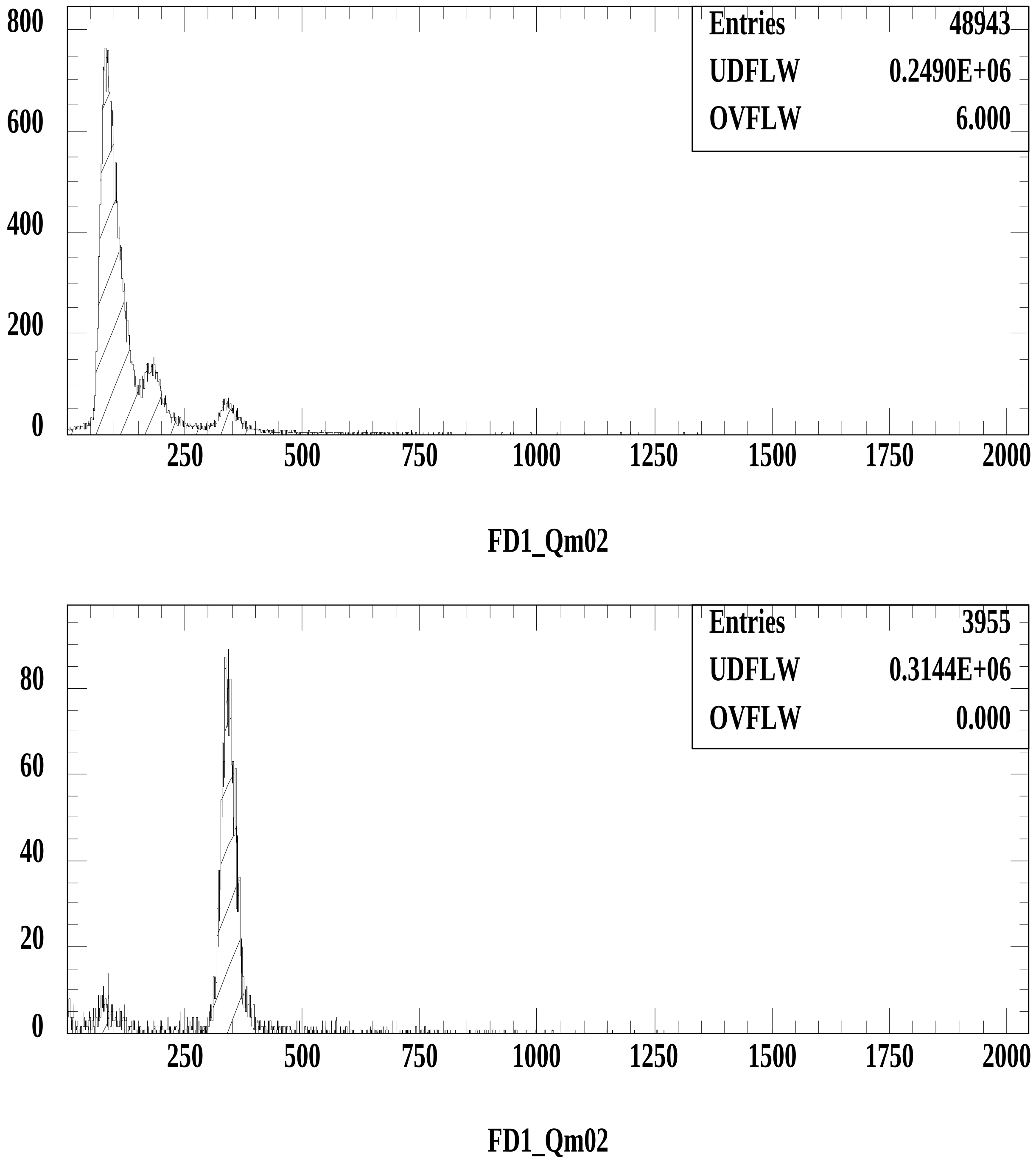

Figure 15: **The amplitude spectra obtained in the FD hodoscope counters in the exposition with the hydrogen cluster target.**
The spectra from counter 2 (close to the beam pipe) of the 1st plane are shown.

Figure 16: empty17

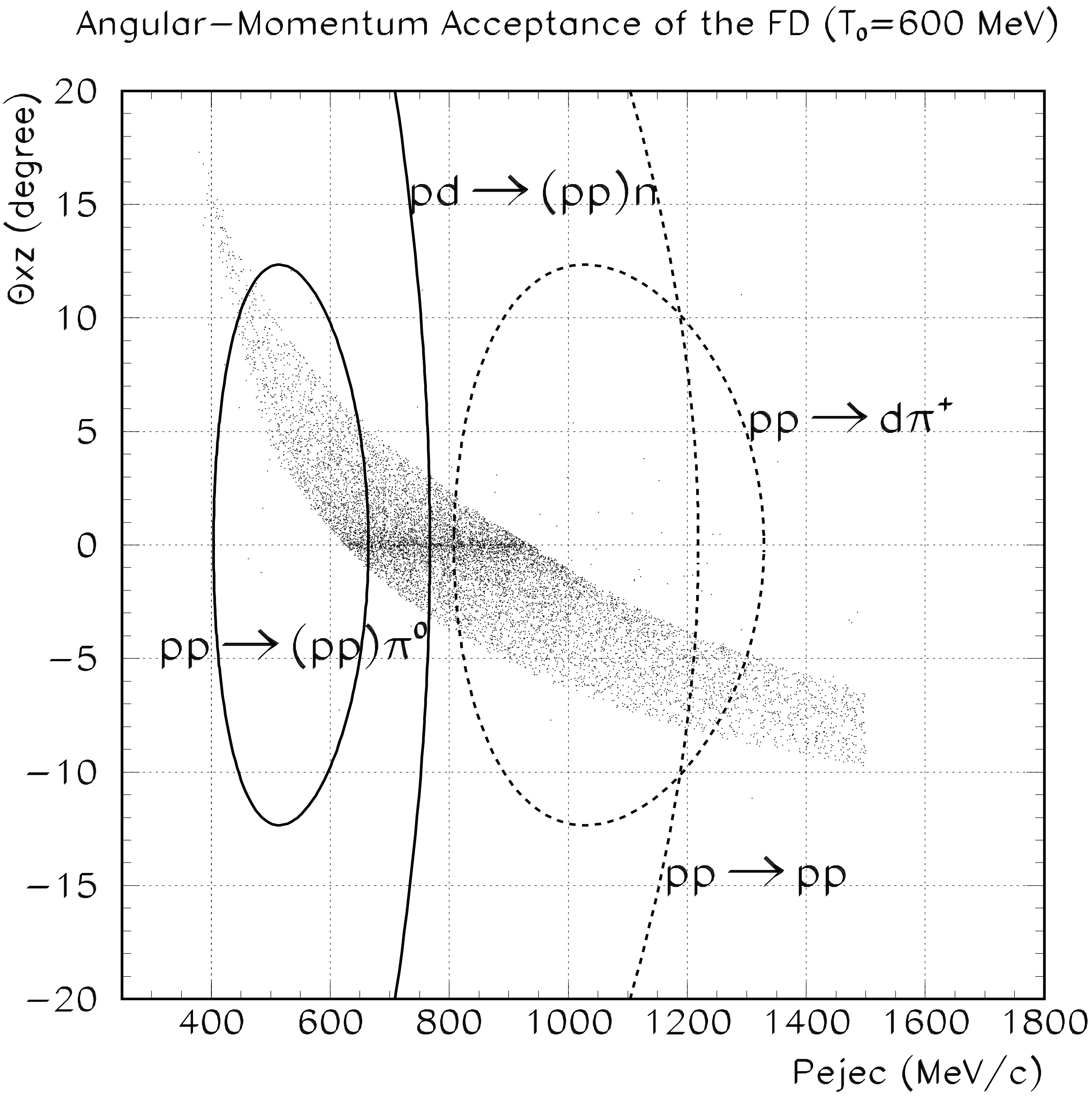

Figure 17: **Angular-momentum acceptance of the Forward Detector at 600 MeV beam energy.**

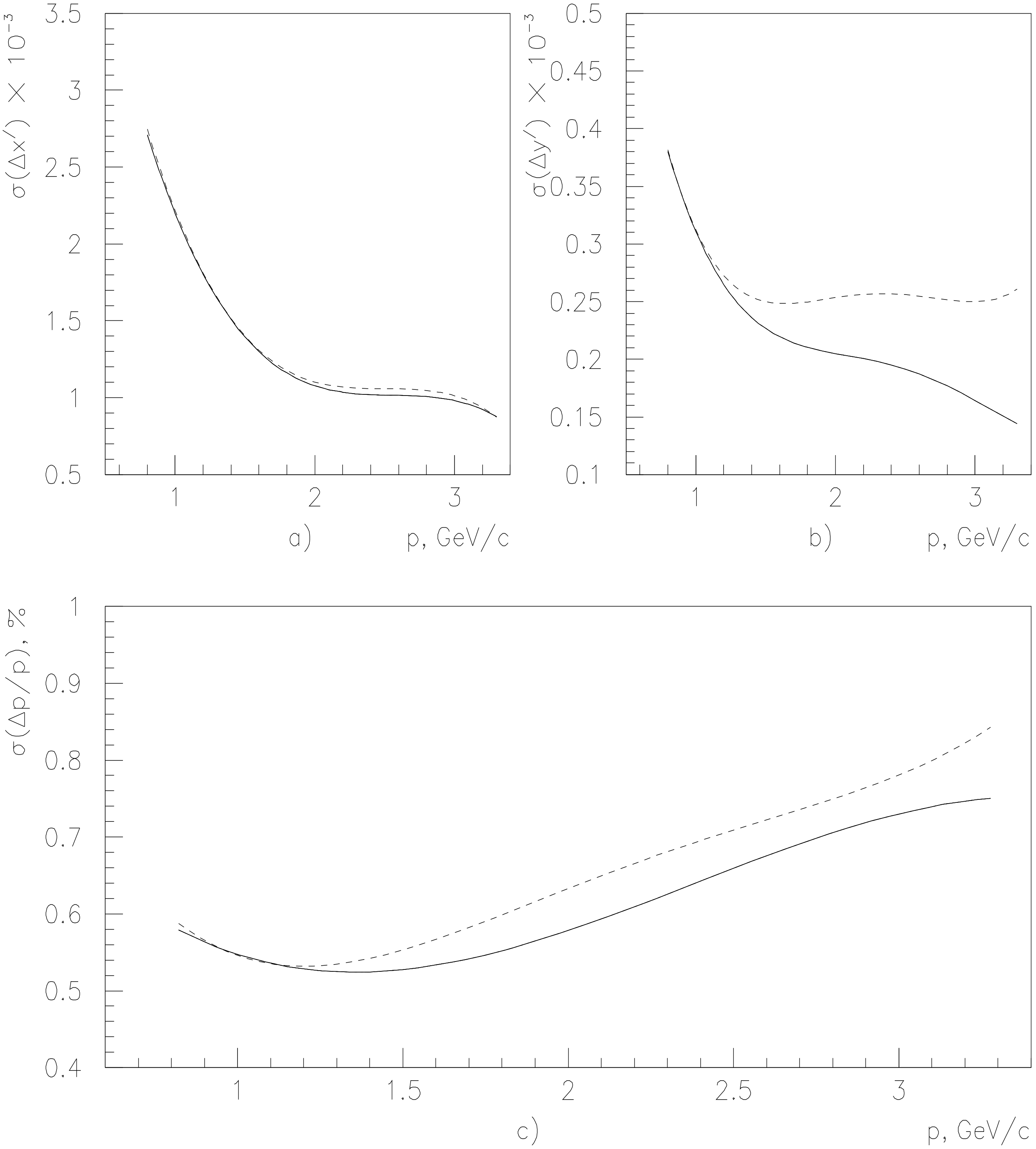

Figure 18: **Expected angular and momentum resolution of the Forward Detector.**

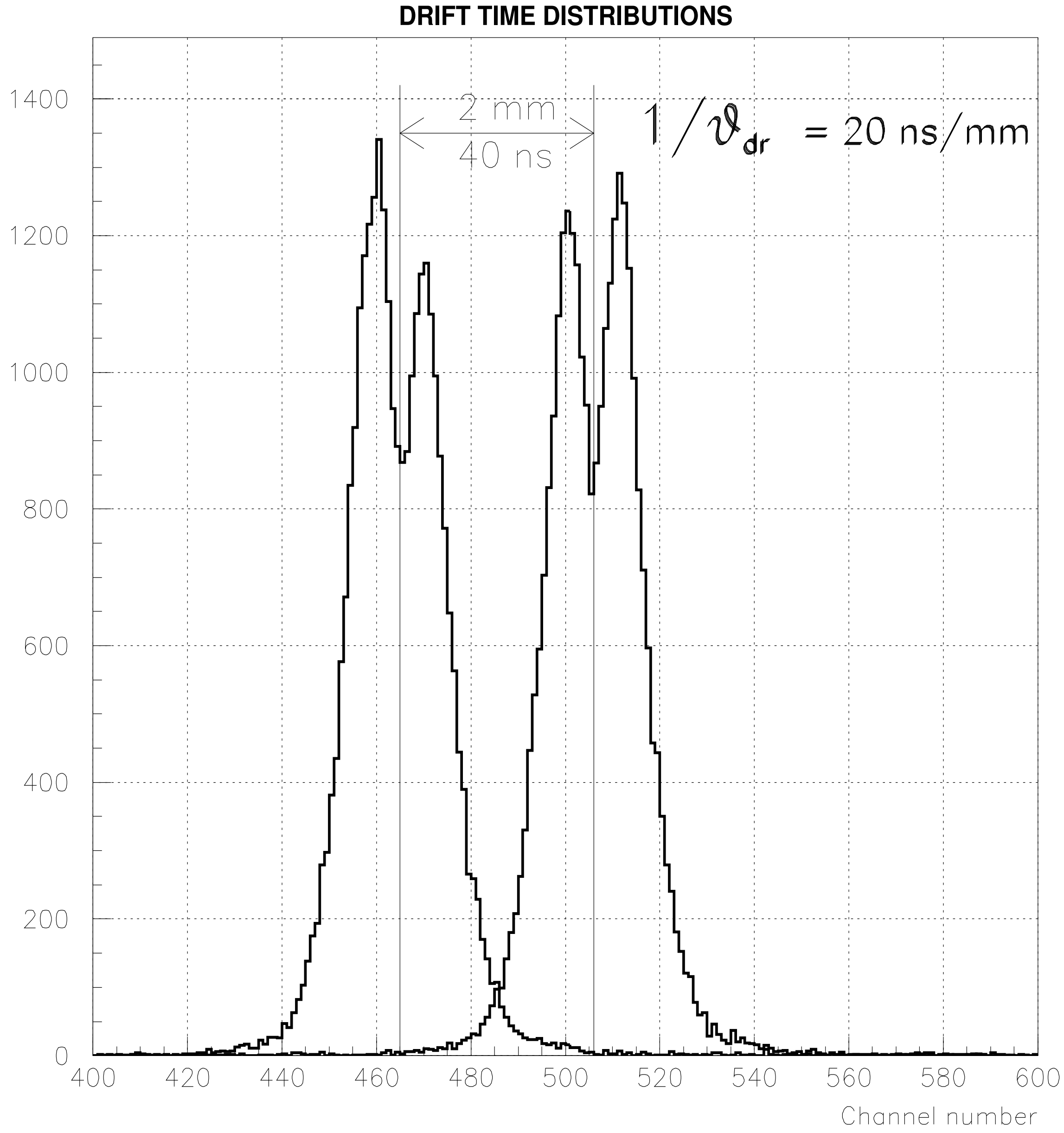

Figure 19: **Backward Drift Chambers test by shadow methode.**
Drift-time distributions measured for 1 anode wire of a backward drift chamber. The dips in the 2 distributions are due to the shadowing of the collimated β - particle beam by 2 adjacent field-forming wires (50 μm diameter, 2.0 mm spacing). The drift velocity results from the measured 20 ns time difference and the 2.0 mm spacing as v_{dr}= 0.05 mm/ns.

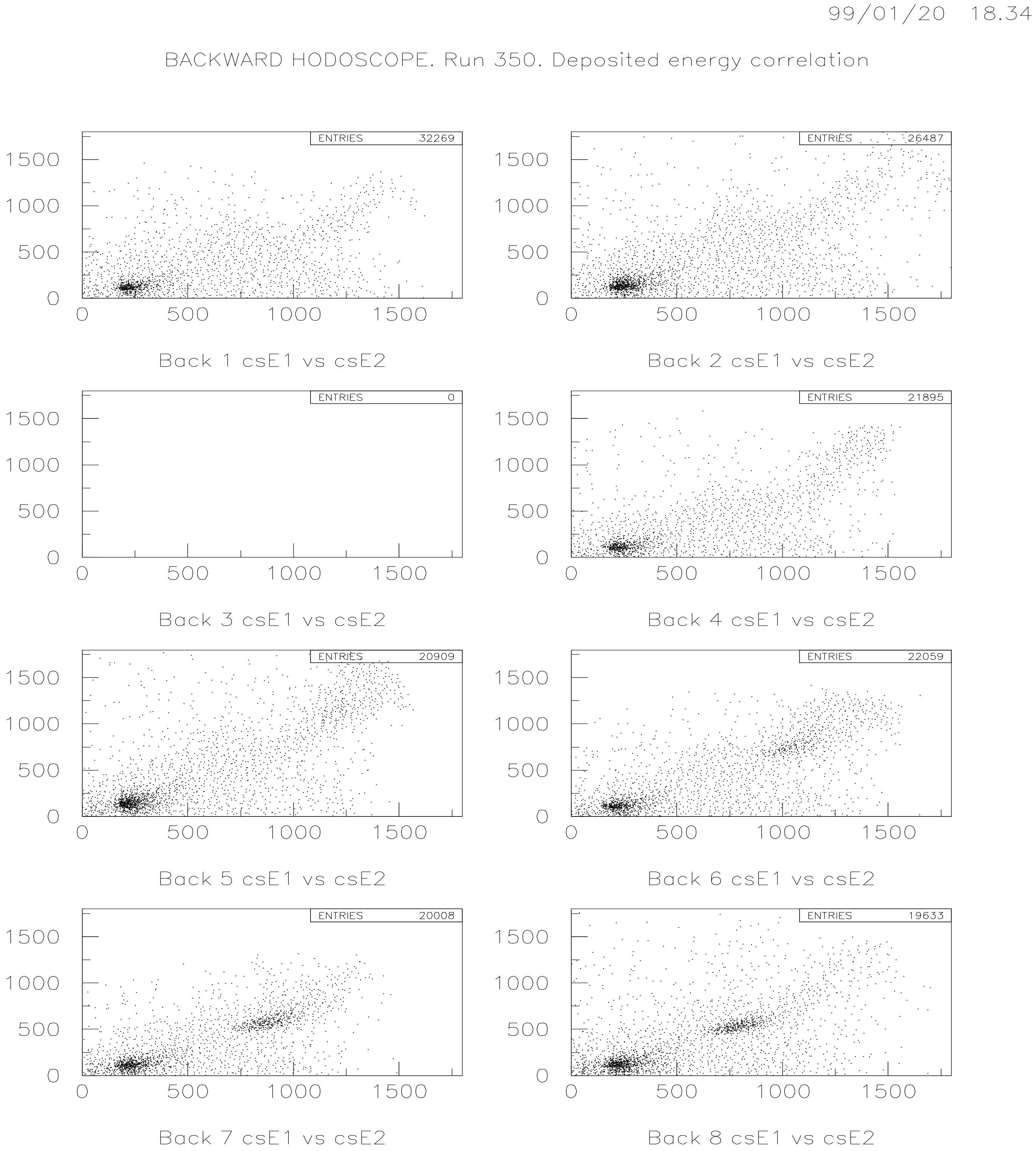

Figure 20: **Backward hodoscope (BH) performance at the beam test.** Amplitude correlation of signals from the counters of the 1-st plane (ordinate) and the 2-nd plane (abscissa). Ejectile momenta going from about 600 MeV/c (upper left, counter 1) to about 200 MeV/c (lower right, counter 8).

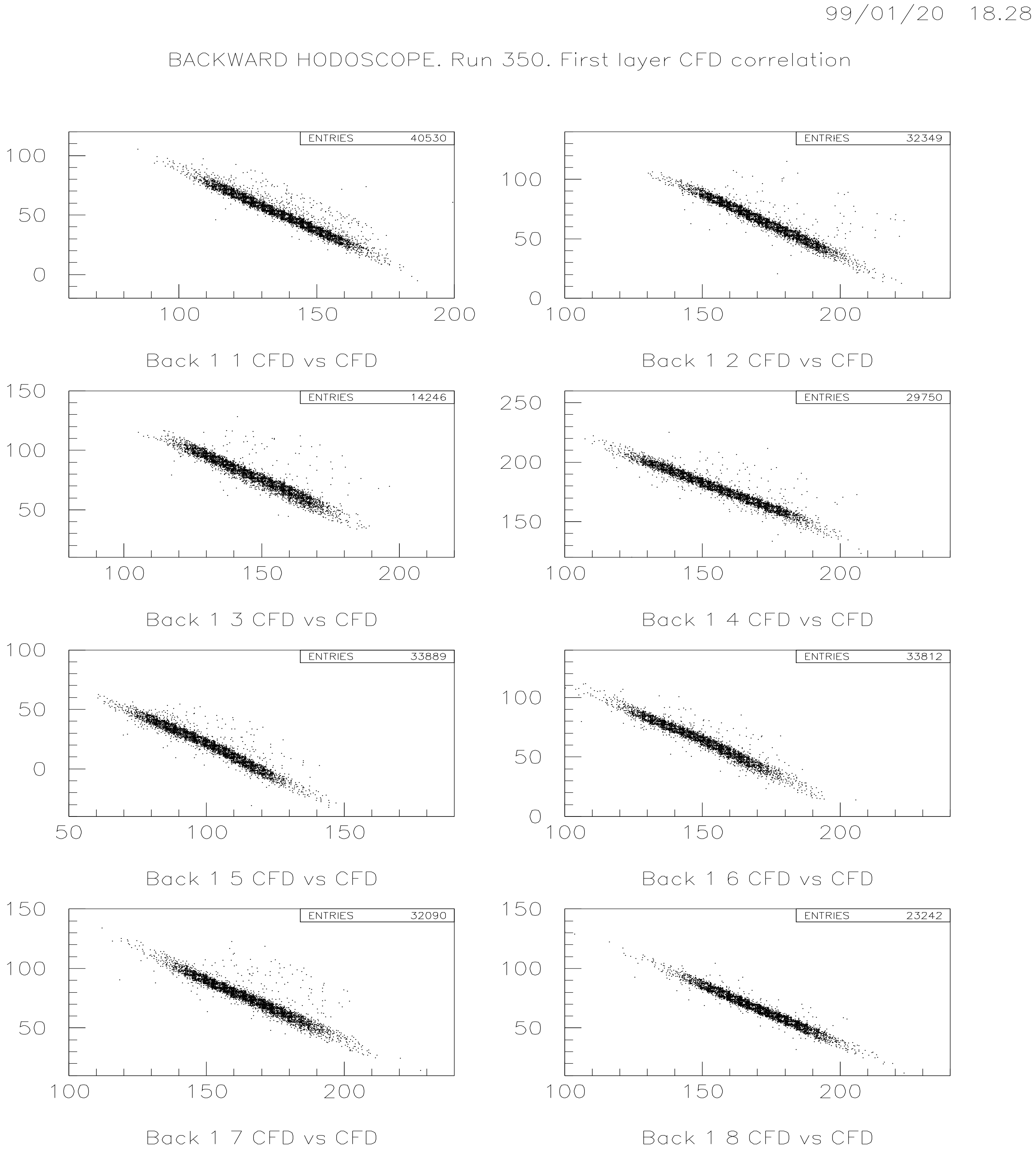

Figure 21: **Backward hodoscope (BH) performance at the beam test.** Time correlation between the signals of upper and lower photomultipliers of the 1-st plane counters to be used for determination of hit position along the counter.

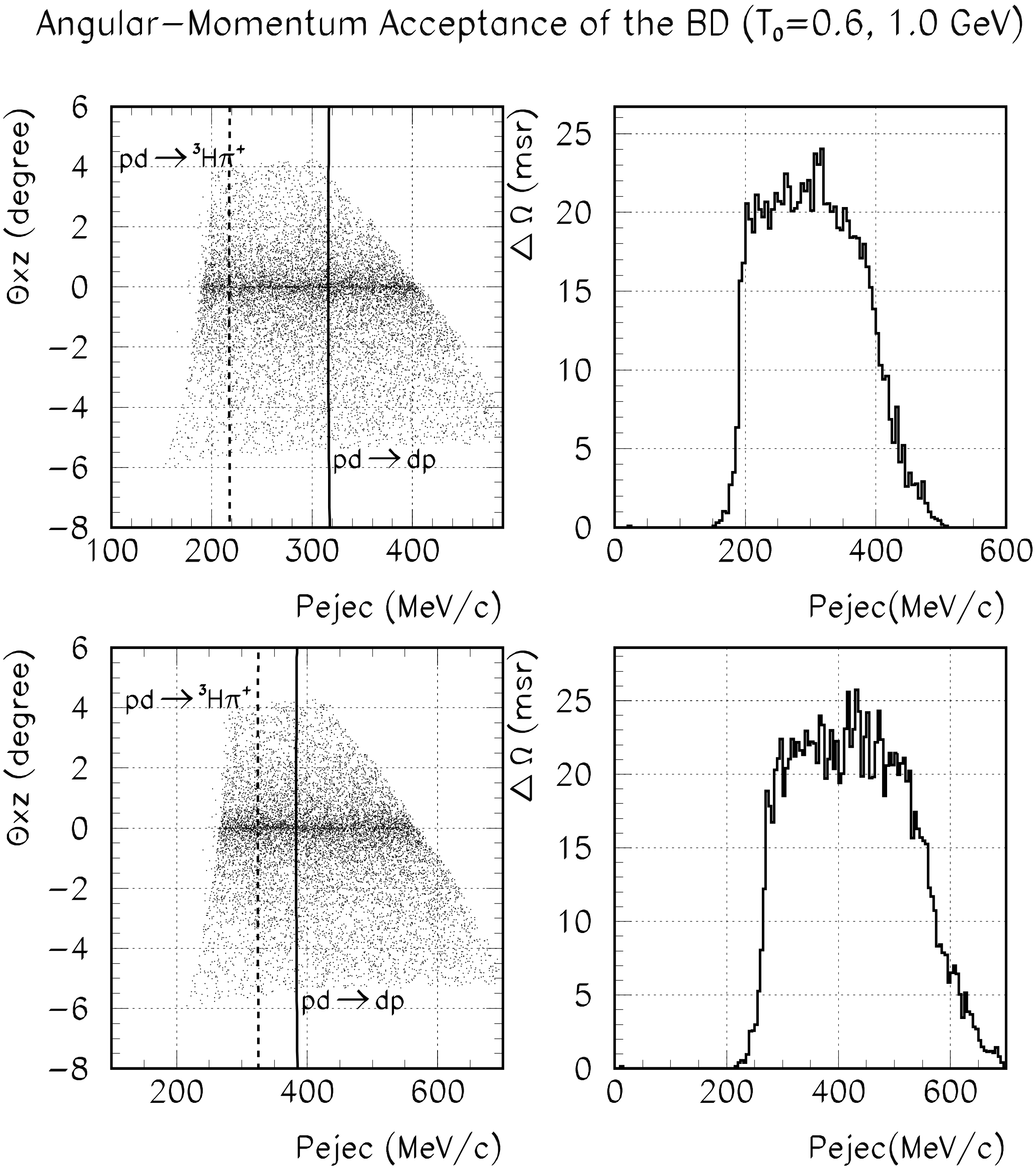

Figure 22: **Angular-momentum acceptance of the Backward Detector (BD).** Beam energy 600 MeV (upper figures) and 1000 MeV (low figures).

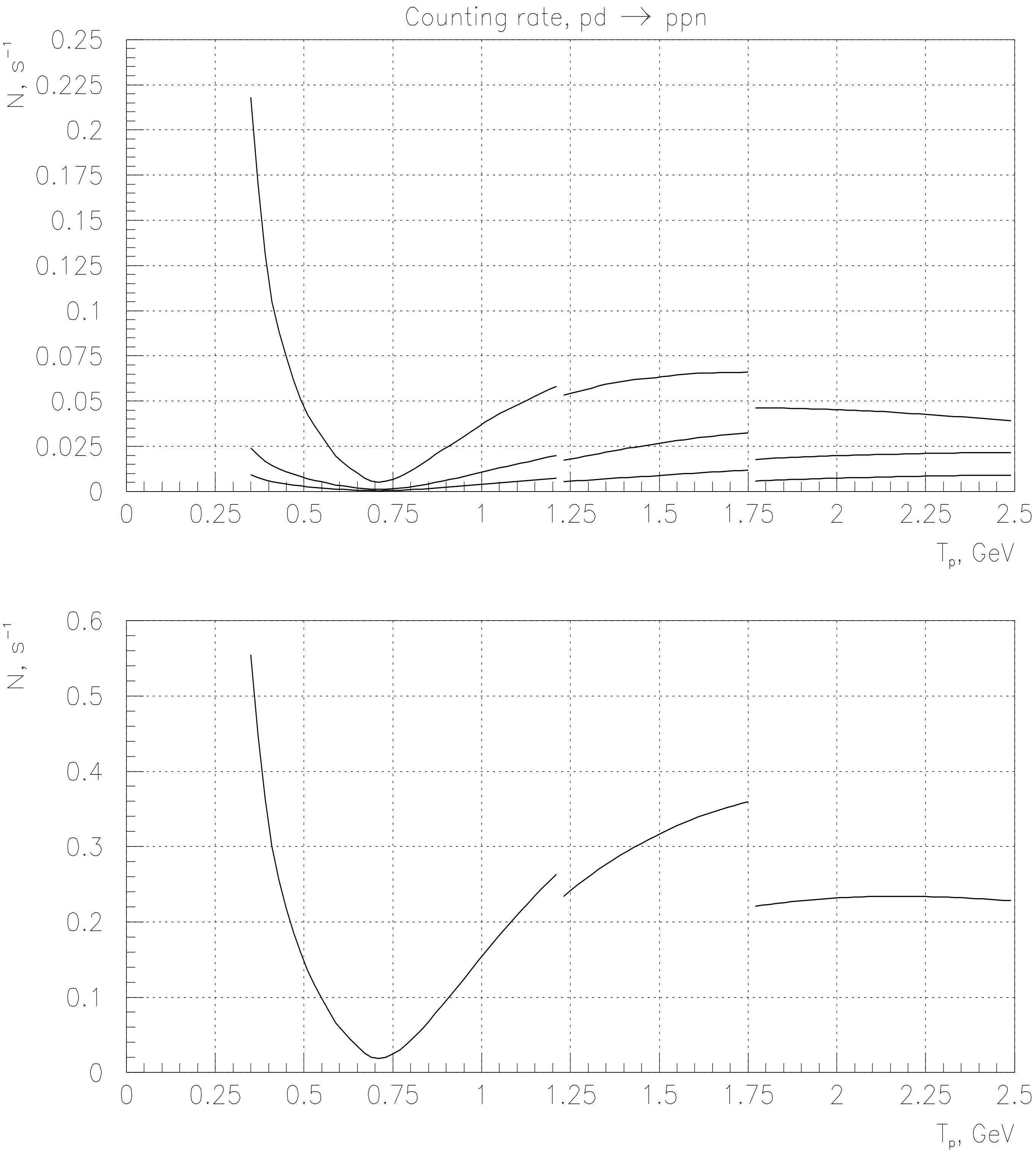

Figure 23: **Count rates for the reaction (1) for different proton pair energies E_{pp} under the assumption of detector efficiency $\varepsilon = 100\%$.**
Upper: $E_{pp} = 0.1$–1.1, 4.1–5.1 and 8.1–9.1 MeV (from top to bottom),
Lower: The sum over E_{pp}= 0....10 MeV.

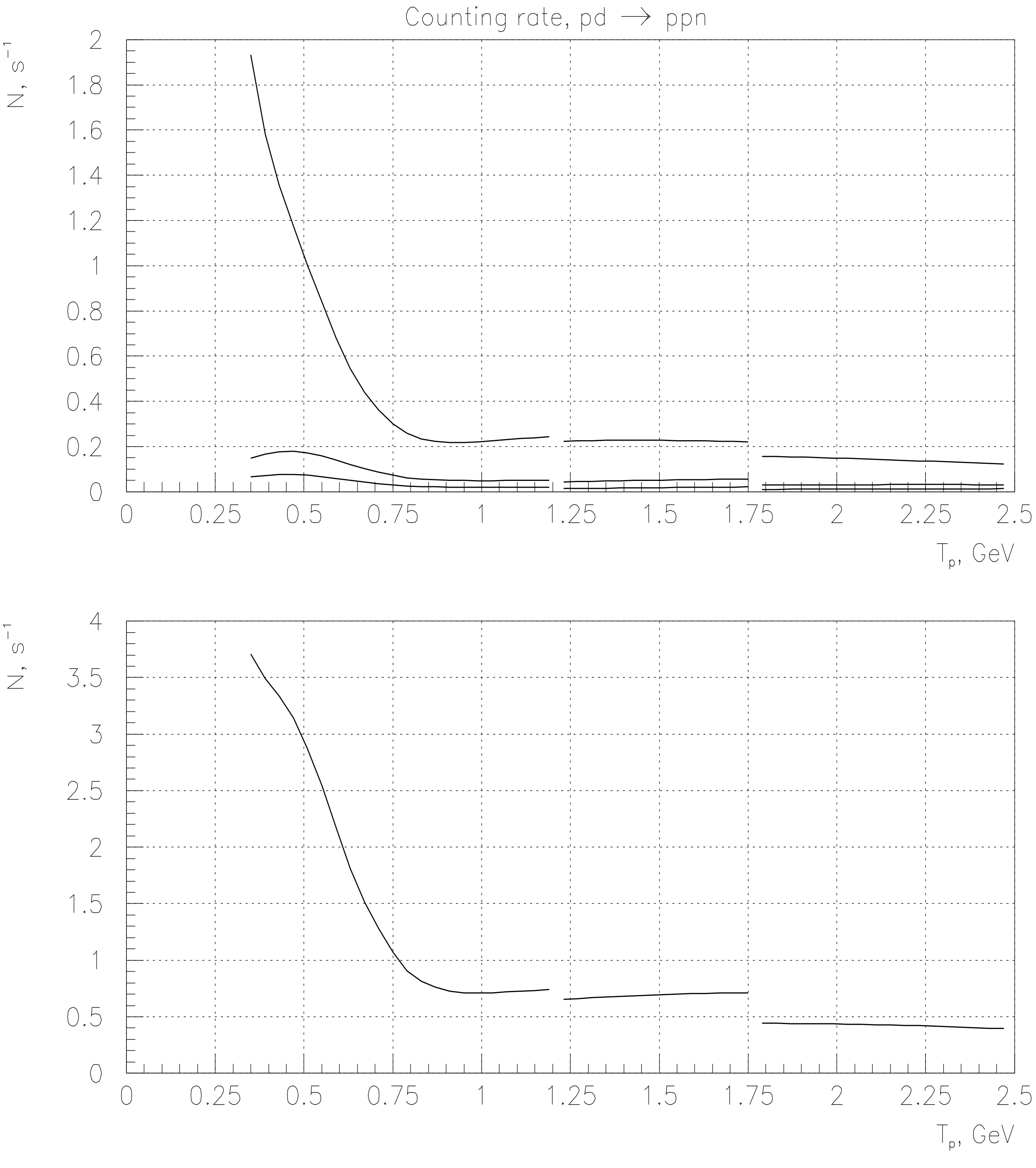

Figure 24: **Count rates for the reaction (2) for different proton-neutron pair energies E_{pn} under the assumption of detector efficiency $\varepsilon = 100\%$.**
Upper: $E_{pn} = 0.1$–1.1, 4.1–5.1 and 8.1–9.1 MeV (from top to bottom),
Lower: The sum over E_{pn}= 0....10 MeV.

Figure 25: **Momentum distribution of particles from the $pd \to ppn$ reaction and background processes detected in the FD hodoscope at $T_p = 1$ GeV.**
Upper: ROC model,
Lower: HBC data.

Figure 26: **Calculated missing-mass spectra for the mesonless break-up and break-up with π^+ production.**
Upper: With the experimental resolution,
Lower: Without the resolution.

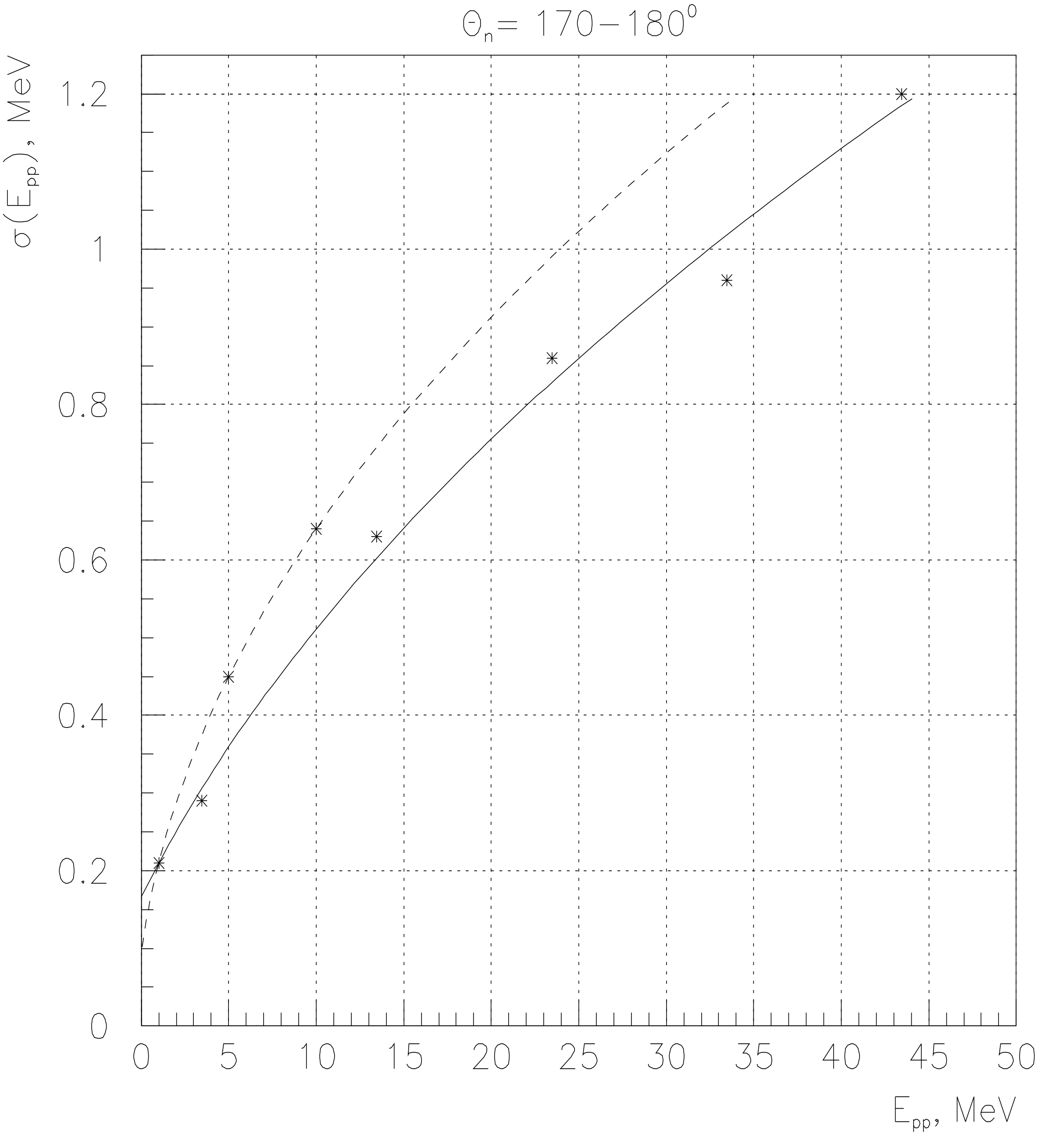

Figure 27: **Resolving power for the proton pair relative kinetic energy.** The solid line is the fit to the calculated points by $\sigma = a \cdot \sqrt{E_{pp}}$. The dashed curve gives the analytic approximation for uncorrelated errors in momentum and angle determination.

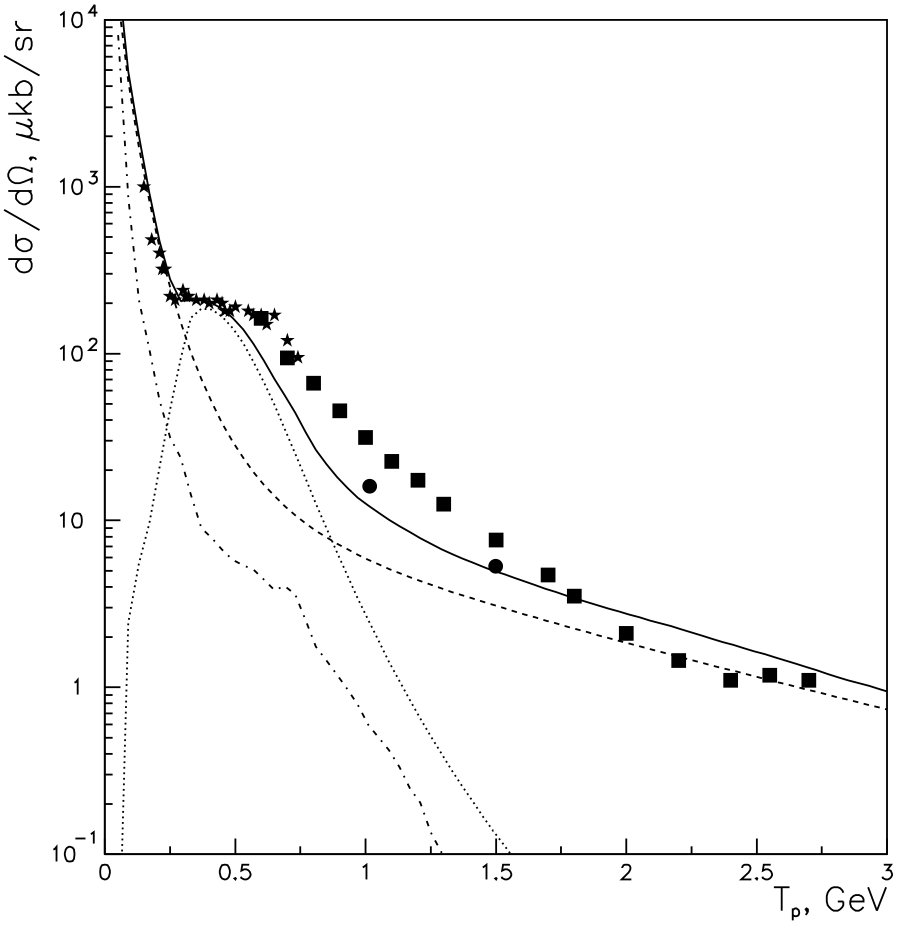

Figure 3: The c.m.s. cross section of the backward elastic pd-scattering at $\theta_{c.m.} = 180^o$ as a function of the laboratory kinetic energy of the incident proton T_p. Curves show the results of calculations [13] with Paris w.f. for different mechanisms — ONE (dashed),SS(dashed-dotted), Δ (dotted), $ONE + \Delta + SS$ (full). Experimental data ($\star$) [27], ($\bullet$) [29], (black squares) [30].

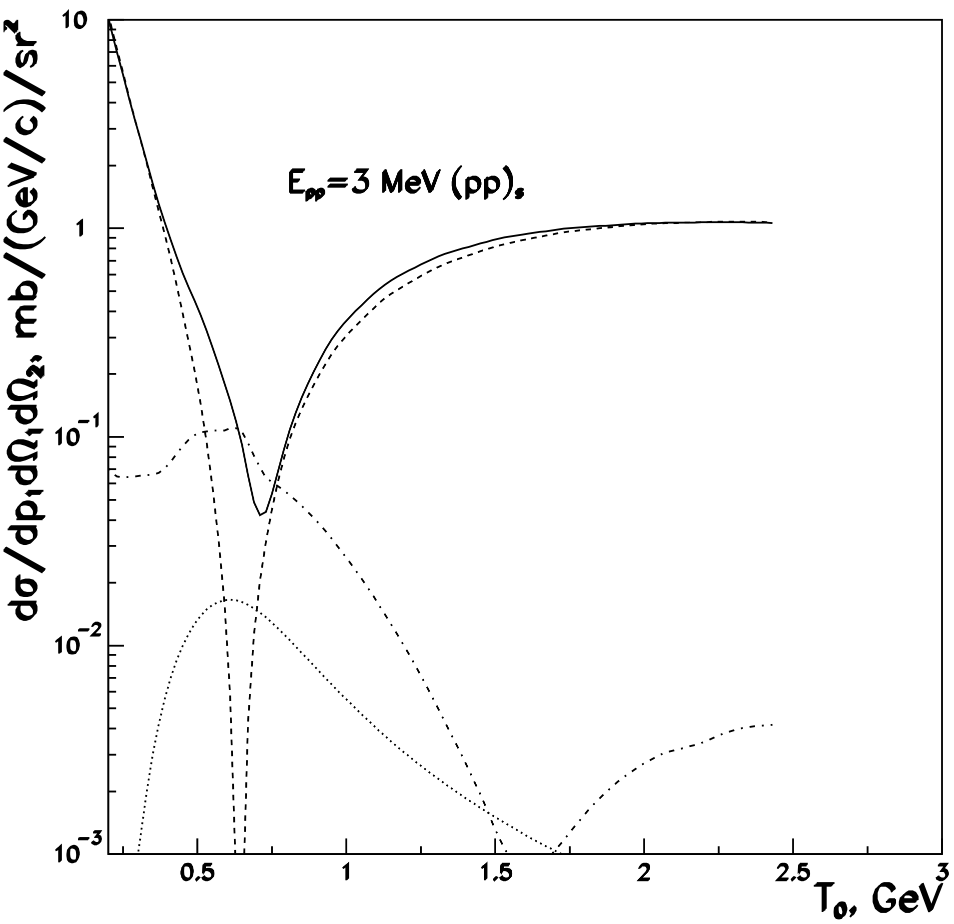

Figure 4: The c.m.s. cross section for the break-up reaction $p+d \to (pp)_s+n$ at $E_{pp} = 3$ MeV (the curves are as in Fig.3)

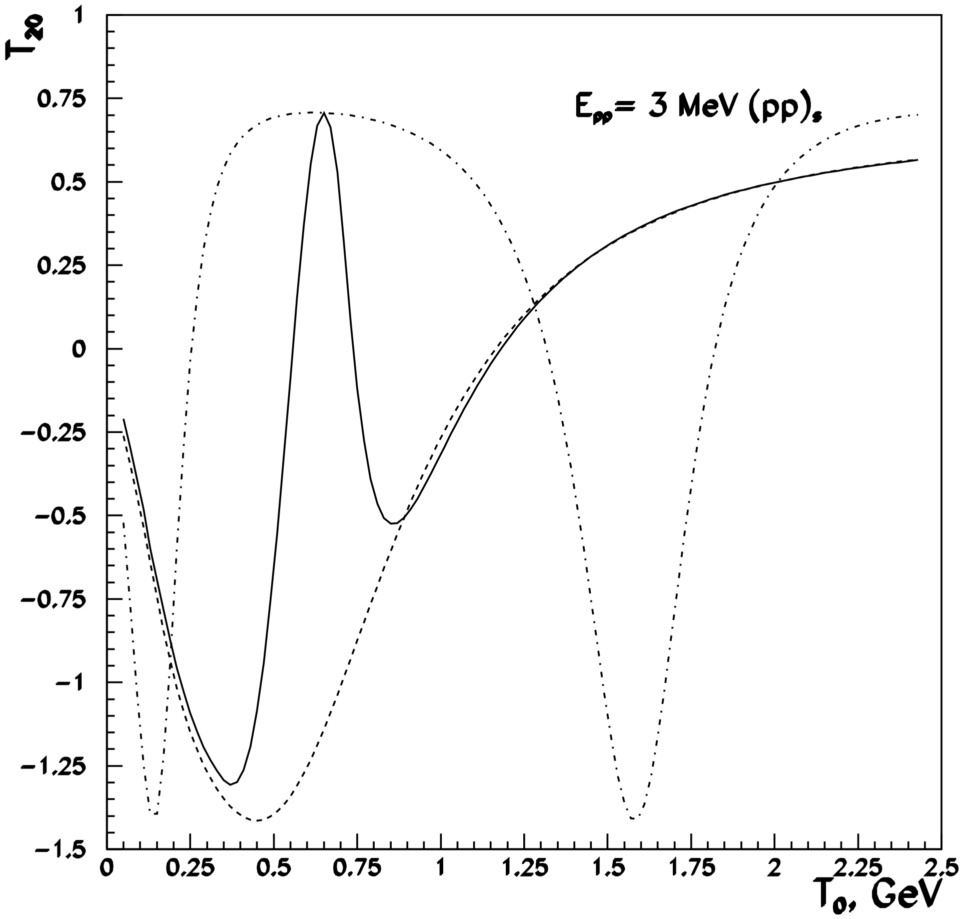

Figure 5: Tensor analyzing power for the reaction $p + d \rightarrow (pp)_s + n$ at $E_{pp} = 3$ MeV calculated in [24] for different mechanisms with RSC w.f. of the deuteron as a function of T_p: ONE (dashed), SS (dash-dotted), ONE+SS (full)

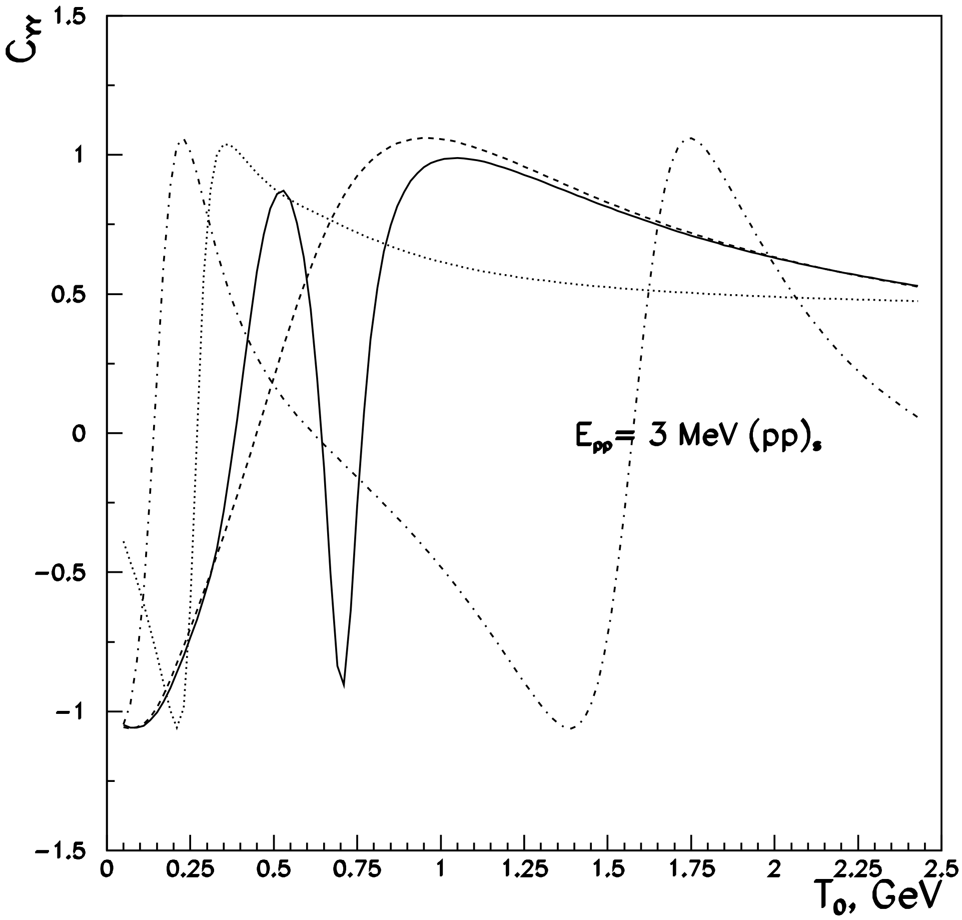

Figure 6: Spin-spin correlation C_{YY} for the reaction $\vec{p} + \vec{d} \rightarrow (pp)_s + n$ at E_{pp} in the same notations as in Fig. 5

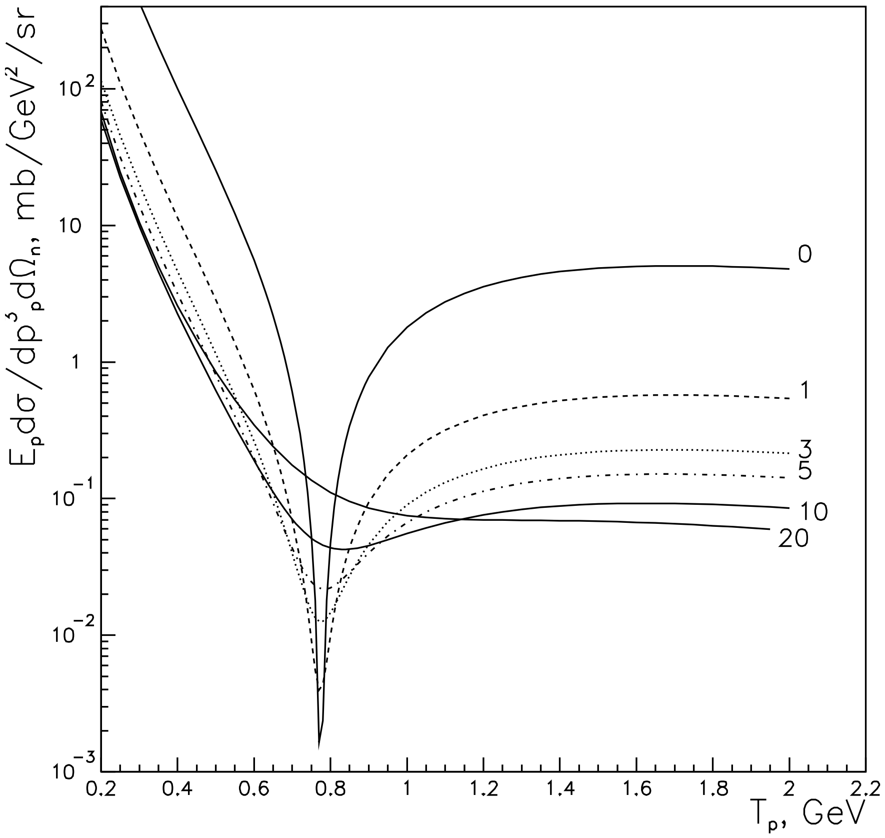

Figure 7: The CMF differential cross section of the reaction $p + d \rightarrow p(0^o) + p + n(180^o)$ as a function of the initial proton kinetic energy in the laboratory frame calculated in Ref. [23] in the framework of the ONE mechanism using Paris potential for the deuteron w.f. and S-, P-, D-, F- and G-waves in the state of the forward going pp-pair. The numbers at the curves denote the energy of relative motion of nucleons in the pair, E_{pp}, in MeV. Coulomb effects in forward $^1S_0$ pair are turned off.

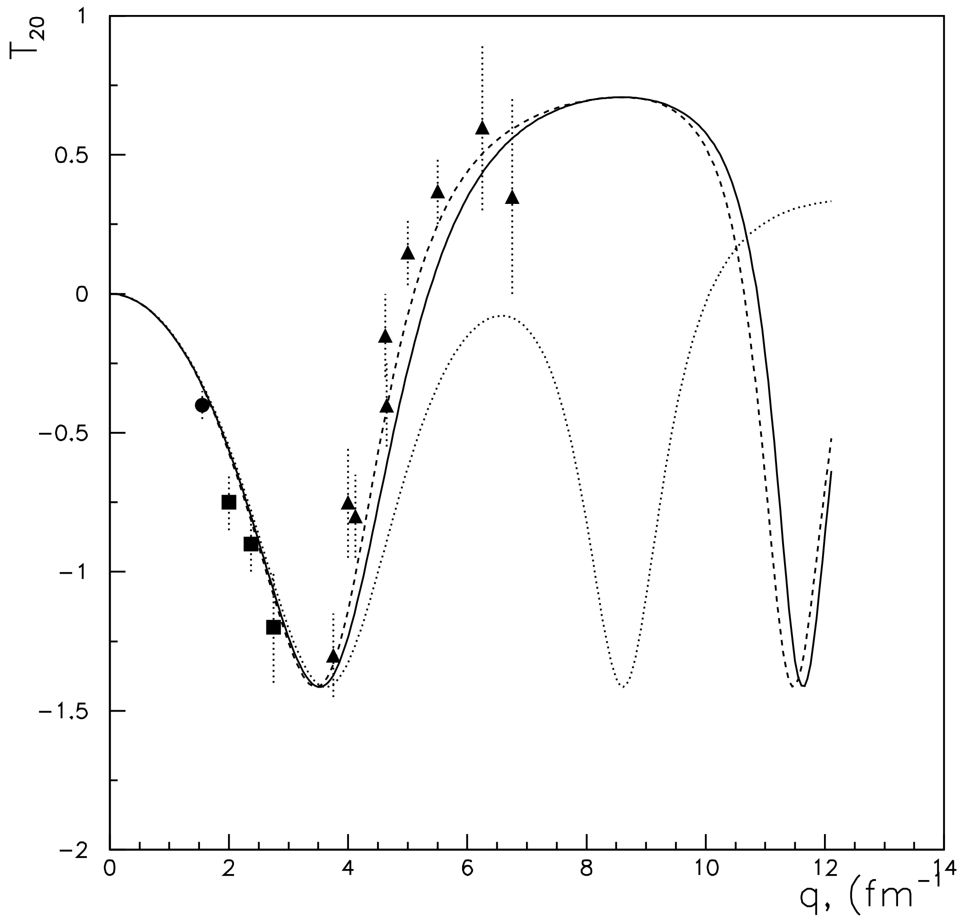

Figure 8: Tensor polarisation T_{20} in elastic ed-scattering as a function of the transferred momentum q. Experimental data are taken from [31]. The curves show the results of nonrelativistic calculation [24] with different w.f. of deuteron — Paris (full), RSC (dashed), deep attractive MSU potential (dotted).

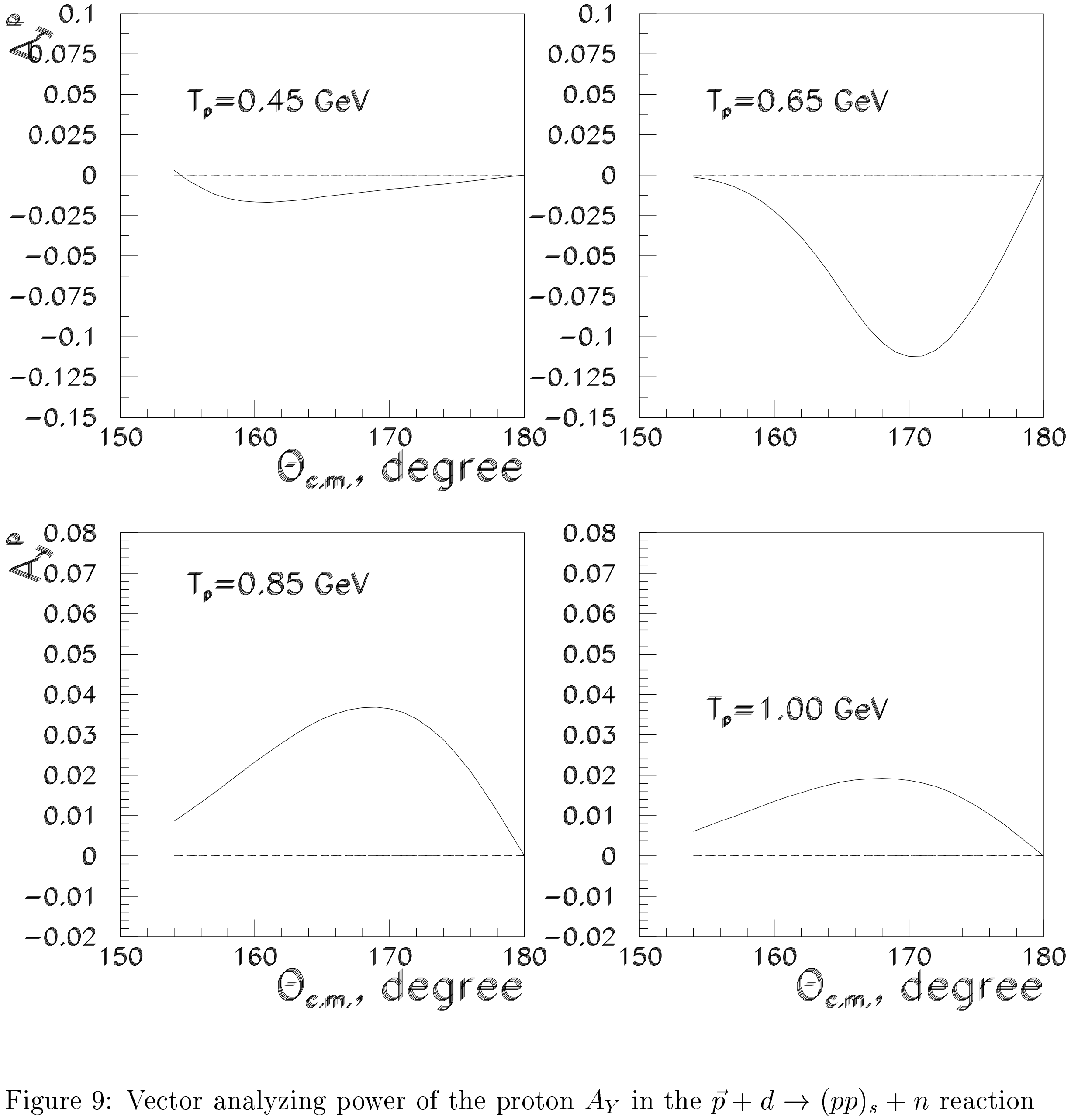

Figure 9: Vector analyzing power of the proton A_Y in the $\vec{p} + d \to (pp)_s + n$ reaction at $E_{pp} = 3$ MeV for different kinetic energies $T_p = 0.45$, 0.65, 0.85 and 1 GeV. Full line presents the result of calculations in the framework of the sum of mechanisms $ONE + \Delta + SS$.

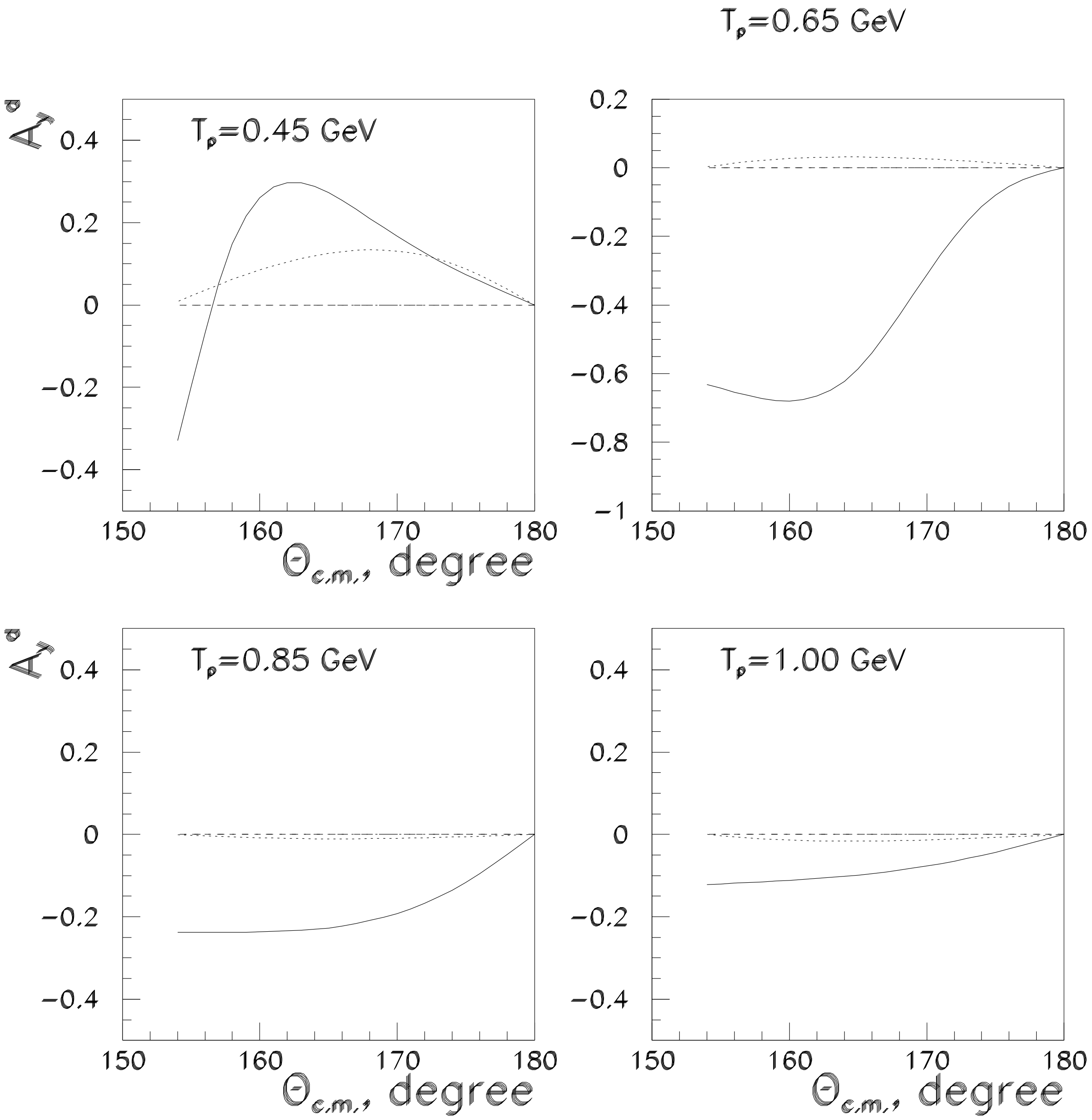

Figure 10: Vector analyzing power of the deuteron A_Y for the $p + \vec{d} \to (pp)_s + n$ at different initial energies calculated for Δ- (dotted) and $ONE{+}\Delta{+}SS$ (full) mechanisms [24].